This is a preprint, the final version is subject to change, of the American Mineralogist (MSA)
Cite as Authors (Year) Title. American Mineralogist, in press.
(DOI will not work until issue is live.) DOI: http://dx.doi.org/10.2138/am-2016-5570

Revision 1

Incorporation of high amounts of Na in ringwoodite: Possible implications for transport of alkali into lower mantle

LUCA BINDI[1,2*], ANASTASIA TAMAROVA[3], ANDREY V. BOBROV[3,4], EKATERINA A. SIROTKINA[3,4], OLIVER TSCHAUNER[5], MICHAEL J. WALTER[6] AND TETSUO IRIFUNE[7,8]

[1] Dipartimento di Scienze della Terra, Università di Firenze, Via La Pira 4, I-50121 Firenze, Italy
[2] CNR - Istituto di Geoscienze e Georisorse, sezione di Firenze, Via La Pira 4, I-50121 Firenze, Italy
[3] Department of Petrology, Geological Faculty, Moscow State University, Leninskie Gory, 119234, Moscow, Russia
[4] Vernadsky Institute of Geochemistry and Analytical Chemistry of Russian Academy of Sciences, Moscow, 119991, Russia
[5] Department of Geoscience and High Pressure Science and Engineering Center, University of Nevada, 4505 S. Maryland Pkwy, Las Vegas, NV 89154, USA
[6] School of Earth Sciences, University of Bristol, Bristol BS8 1RJ, UK
[7] Geodynamics Research Center, Ehime University, Matsuyama 790-8577, Japan
[8] Earth-Life Science Institute, Tokyo Institute of Technology, Tokyo 152-8550, Japan

E-mail address: luca.bindi@unifi.it

ABSTRACT

Here we report on the coexistence between Na-rich ringwoodite and bridgmanite in the system $MgSiO_3$-Na_2CO_3-Al_2O_3 at 24 GPa and 1700 °C. In our experiments ringwoodite incorporates up to 4.4 wt% Na_2O, with Na entering the octahedral site together with Si, according to the mechanism: $Mg^{2+} \rightarrow \frac{2}{3}Na^{+} + \frac{1}{3}Si^{4+}$. The volume of the unit-cell increases along with the Na content. A similar behavior is observed for the unit-cell volume of Na-bearing bridgmanite, although the mechanism of Na incorporation into this structure remains unknown because of the lack of sufficient crystallographic data. Na_2O is compatible in ringwoodite relative to bridgmanite with a partition coefficient (D) of 5 (+5/-4), but is incompatible in ringwoodite relative to carbonate rich melt/fluid, with the D value ranging between 0.5 and 0.1. Al is highly enriched in bridgmanite relative to the other coexisting phases. Carbonatitic melt metasomatism in the deep transition zone may lead to local Na-enrichment, and ringwoodite may be an important host for Na in the deep transition zone. Subsequent convection or subduction of metasomatised mantle may lead to enrichment of alkaline elements in the upper and lower mantle.

Keywords: ringwoodite, bridgmanite, sodium, spinel, crystal structure, microprobe analysis, alkalis

INTRODUCTION

Spinel group minerals have very compact structures based on a slightly distorted closed packed oxide anion lattice. While there are a large number of spinels with different

compositions, the compatibility of elements in a given spinel is quite limited by its constituent ions and the rigidity of the densely occupied lattice, with only two structural degrees of freedom, the oxygen *u* parameter and inversion (e.g., Hill et al. 1979; O'Neill and Navrotsky 1983). Consequently, large monovalent cations like Na and K are not expected to exhibit high solubility in Mg_2SiO_4 ringwoodite in the spinel structure. Ringwoodite-ahrensite (Mg_2SiO_4-Fe_2SiO_4) solid solution is the major rock-forming mineral in peridotitic lithologies in the deep transition zone. Ringwoodite can incorporate a considerable amount of hydrogen into its structure (e.g., Smyth et al. 2003), and the deep transition zone may have a storage capacity of several weight percent water (e.g., Ohtani et al. 2004). Estimates of the electrical conductivity in the transition zone argue for an overall modest amount of water (Yoshino et al. 2008; Karato 2011), whereas recently an inclusion of ringwoodite in diamond was found to contain up to 4000 ppm of water (Pearson et al. 2014). These two findings are not necessarily in contradiction. Water- and CO_2-bearing fluids, perhaps derived from subducted material, may cause local heterogeneity in the mantle. This is known to be the case in the upper mantle, where fluid-driven mantle metasomatism is a common and geochemically important process (Haggerty 1983; Yaxley et al. 1991; Ionov et al. 1997; Gregoire et al. 2002). Diamonds with mineral inclusions originating in the transition zone and lower mantle provide strong evidence for the involvement of such fluid- or melt-driven processes (Walter et al. 2008; Bulanova et al. 2010; Harte 2010), and it is likely that diamonds form by reduction of carbon-bearing fluids (Rohrbach and Schmidt 2011). Fluid-driven metasomatism in the upper mantle is known to selectively mobilize incompatible elements, thus creating mantle regions that are depleted or enriched in those elements.

In order to better understand the crystal-chemical behavior of sodium, and by proxy other monovalent alkali elements, in the deep transition zone, we made a series of experiments on a simplified chemical system involving a Na-rich carbonated melt and mantle silicate. Experiments were conducted at 24 GPa, 1700 °C, thus representing conditions at the border between the transition zone and lower mantle.

EXPERIMENTAL DETAILS

Synthesis

An experiment at 24 GPa and 1700 °C was performed using a 2000 ton split-sphere press installed at the Ehime University (Matsuyama, Japan). The sample was compressed by eight cubic tungsten carbide anvils with 2.5 mm truncation edge lengths, and with pyrophyllite as gasketing material. A Co (17 wt%)-doped MgO octahedral pressure medium of 8 mm edge length was compressed using eight cubic tungsten carbide anvils with 3 mm

truncation edge lengths. Pyrophyllite gaskets, 4 mm in width, were used to seal the compressed volume and support the anvil flanks. Heating of the sample was performed by a cylindrical $LaCrO_3$ heater, 3.2/2.0 mm in outer/inner diameter and 4 mm in length. Approximate sample volumes after experiments were 1.0 mm^3. A starting mixture of oxides and carbonate [MgO (40 mol%) + SiO_2 (35 mol%) + Na_2CO_3 (20 mol%) + Al_2O_3 (5 mol%)] was dried for a few days at a temperature of 105 °C and kept in a dessicator. Temperature during the experiment was controlled by a $W_{97}Re_3$-$W_{75}Re_{25}$ thermocouple, 0.1 mm in diameter. The pressure was calibrated at room temperature using the semiconductor-metal transitions of Bi, ZnS and GaAs (Irifune et al. 2004). The effect of temperature on pressure was further corrected using the α-β and β-γ phase transitions of olivine (Katsura and Ito 1989). The run duration was 15 minutes. In the run product (Fig. 1), Na-ringwoodite (Na-rgw) coexists with abundant (microcrystalline) Na-bearing bridgmanite (Na-brg), minor periclase and quenched carbonate-silicate melt in the interstitial spaces. The roughly estimated proportions of the phases (by SEM area fractions; in vol. %) are: bridgmanite (75), ringwoodite (15), Na-free periclase (5), carbonate-silicate melt (5).

Chemical Composition

The chemical compositions of ringwoodite and bridgmanite were determined by wavelength dispersive analysis (WDS) using a Jeol JXA-8600 electron microprobe with 10 kV and 10 nA as voltage and current settings. Signal was accumulated over 40 s for each element. The standards employed were forsterite (Mg, Si) and albite (Na, Al). The selected fragments (3 Na-rgw and 2 Na-brg, all tested by X-ray diffraction) were found to be homogeneous within the analytical uncertainty. Fe was found to be below the detection limit (0.02%). The average chemical compositions are given in Table 1. Periclase was found to be pure MgO. The coexisting melt showed the following composition (average of 3 spots; wt% of oxides): 21.7(2) (Na_2O), 20.7(1) (MgO), 2.29(3) (SiO_2), 1.32(4) (Al_2O_3) and 54.0(3) (CO_2). Additional chemical analyses of the phases in the experimental run were obtained by means of a Zeiss - EVO MA15 Scanning Electron Microscope coupled with an Oxford INCA250 energy-dispersive spectrometer, operating at 15 kV and 5 kV accelerating voltage, 500-150 pA probe current, 2,500 cps as average count rate on the whole spectrum, and a counting time of 500 s. The lower voltages were used in order to minimize secondary radiation from adjacent phases. The results of the all the chemical analyses obtained for Na-rgw and Na-brg are graphically reported in Figure 2.

X-ray single-crystal diffraction

Numerous Na-rgw crystals, hand-picked under a reflected light microscope from the run product (Fig. 1), were preliminarily examined with a Bruker-Enraf MACH3 single-crystal

diffractometer using graphite-monochromatized Mo*K*α radiation and with an Oxford Diffraction Xcalibur 3 diffractometer (X-ray Mo*K*α radiation, λ = 0.71073 Å) equipped with a Sapphire 2 CCD detector. Most of the crystals were found to be composed of minute aggregates. Diffraction peaks were broad and rather weak. For two crystals (20 × 30 × 35 μm in size, approximately) it was possible to get the unit-cell parameters only: 8.090(1) (Na-rgw2) and 8.085(1) Å (Na-rgw3). No full data collection of the Ewald sphere was obtained. Finally, a Na-rgw crystal (Na-rgw1; Table 2) with appropriate diffraction quality was found and the full data collection was done with an Oxford Diffraction Xcalibur 3 diffractometer (X-ray Mo*K*α radiation, λ = 0.71073 Å) equipped with a Sapphire 2 CCD detector. Intensity integration and standard Lorentz-polarization corrections were performed with the *CrysAlis* RED (Oxford Diffraction 2006) software package. The program ABSPACK of the *CrysAlis* RED package (Oxford Diffraction 2006) was used for the absorption correction. Reflection conditions were consistent with the space group $Fd\bar{3}m$, the space group typically observed for spinel phases. The full-matrix least-squares program SHELXL-97 (Sheldrick 2008), working on F^2, was used for the refinement of the structure, which was carried out starting from the atomic coordinates reported by Ye et al. (2012) for pure Mg_2SiO_4 ringwoodite. Site-scattering values were refined using scattering curves for neutral species (Ibers and Hamilton 1974) as follows: Mg vs. (where the symbol stands for structural vacancy) for the octahedral site, Si for the tetrahedral site, and O vs. for the anion site. All the sites were found fully occupied, and the occupancy factors were then fixed to 1.00. The electron density refined at the metal sites is in excellent agreement with the electron microprobe data. In detail, the mean electron number at the octahedral site is 12.0 (pure Mg), well matching the site population obtained at the microprobe ($Mg_{0.85}Na_{0.10}Si_{0.05}$; e^- = 12.00). Such a distribution reflects well on the bond distances observed. Successive cycles were run introducing anisotropic temperature factors for all the atoms leading to R_1 = 0.0319 for 67 observed reflections [$F_o > 4\sigma(F_o)$] and R_1 = 0.0321 for all 86 independent reflections (Table 2). Fractional atomic coordinates, atomic displacement parameters and bond distances are given in Table 3. The list of the observed and calculated structure factors and the CIF are deposited[1].

Six Na-brg fragments were mounted on a 0.005 mm diameter carbon fiber (which was, in turn, attached to a glass rod) and checked on both a CCD-equipped Oxford Diffraction

[1] For a copy of the list of observed and calculated structure factors and CIF, document item AMxxxxx, contact the Business Office of the Mineralogical Society of America (see inside front cover of recent issue) for price information. Deposit items may also be available on the American Mineralogist web site at http://www.minsocam.org.

Xcalibur 3 single-crystal diffractometer, operating with Mo*K*α radiation (λ = 0.71073 Å), and an Oxford Diffraction Xcalibur PX Ultra diffractometer equipped with a 165 mm diagonal Onyx CCD detector at 2.5:1 demagnification operating with Cu*K*α radiation (λ = 1.5406 Å). No diffraction spots were detected. Two fragments consisted of many tiny grains and thus four diffraction rings were collected. We were able to calculate the unit-cell volume for these two grains: $V = 166(1)$ Å^3.

RESULTS AND DISCUSSION

The structure of Na-rgw was found to be topologically identical to those reported for pure Mg_2SiO_4 (Ye et al. 2012). The mean octahedral metal-oxygen distance of 2.088(1) Å is greater than that observed for pure Mg_2SiO_4 (2.072 Å; Ye et al. 2012) in keeping with the presence of Na. On the basis of the reaction $Mg^{2+} \rightarrow \frac{2}{3}Na^{+} + \frac{1}{3}Si^{4+}$, substitution of twice the amount of Na with respect to Si results in an increase of the octahedral volume [12.01 Å^3 in Na-rgw1 with respect to 11.81 Å^3 in pure Mg_2SiO_4 (Ye et al. 2012)], although we expect a compensation of the octahedral bond distance due to the presence also of silicon at the site. Thus, the formula of Na-bearing ringwoodite can be written as $(Mg_{1-3x}Na_{2x}Si_x)_2SiO_4$, with x = 0.050, 0.030 and 0.015, for Na-rgw1, Na-rgw2 and Na-rgw3, respectively. Substitution of the large Na cation in the octahedral site induces a shortening of the <T-O> bond distance (1.645 Å) with respect to that observed in pure Mg_2SiO_4 (<T-O> = 1.663 Å, Ye et al. 2012). This feature is not surprising given the strong relationships between octahedral and tetrahedral sites among silicates. This is a consequence of the rigidity of the oxide sublattice, which has only one structural parameter of freedom on site 32*e* that couples tetrahedral and octahedral bond distances (though it may be mediated by inversion, which is not observed here). In fact, the *u*-parameter of site 32*e* can be calculated from the average M-O and T-O bond distances (O'Neill and Navrotsky 1983). Deviations between measured and calculated *u* parameter has been found to be within uncertainty of *u* for almost all spinels (Hill et al. 1979). For Na-rich ringwoodite, and in contrast to Na-free ringwoodite (Hazen et al. 1993), *u* deviates significantly from the expected trend (Fig. 3). For ahrensite (Ma et al. 2015) a deviation is possible within uncertainties. Such deviation of *u* indicates sublattice disorder through local deviation of cations (M-site) from 16*d*. This provides a plausible explanation for the observed Na incorporation. 16*d* sites with Na and Si are indeed more distorted (σ^2 = 12.21; Robinson et al. 1971) than pure Mg sites (σ^2 = 8.17; Ye et al. 2012), yet there is no net deviation for the overall structure.

The effect of Na in the ringwoodite structure is also apparent in the unit-cell parameter which increases to 8.0952(3) in Na-rgw with respect to 8.0816 in pure Mg_2SiO_4 (Ye et al.

2012). If we consider the Na contents (in atoms per formula unit) versus the unit-cell parameters obtained for the three Na-rgw crystals, we can efficiently model the effect of the incorporation of sodium in the ringwoodite structure. The data can be fitted by the following linear equation (R^2 = 0.999): a (Å) = 8.0815(1) + 0.068(1)*Na (a.p.f.u.).

The unit-cell volume observed for Na-bearing bridgmanite [166(1) Å^3] is larger than that observed for pure $MgSiO_3$ [162.53(1) Å^3, Dobson and Jacobsen 2004], due to the presence of the large Na cation. However, the mechanisms of Na incorporation in this structure remain unknown. Indeed, the chemical compositions obtained are not charge balanced: Na replaces Mg and Al replaces Si giving rise to an undercharged chemical formula (when the data are normalized to 3 oxygen atoms; Table 1). A possible solution could be a partial oxygen vacancy, as commonly observed in O-deficient perovskites, but these considerations must await the availability of suitable single crystals for careful X-ray investigations.

IMPLICATIONS

Our results indicate a remarkably high solubility of Na in ringwoodite in presence of a carbonaceous fluid. This has implications for transport of alkali in the deep mantle. Our analyses show that the ringwoodite/carbonate melt partition coefficient for Na_2O is ~ 0.1–0.5 (in wt%) in the chemical system we investigated. Although Na remains incompatible in ringwoodite, this relatively high partition coefficient suggests that under certain conditions ringwoodite could act as an important host for Na, and perhaps K, in the deep transition zone.

Walter et al. (2008) have argued that low-degree melts from carbonated eclogite in the transition zone are recorded in the observed trace element abundances in majoritic garnet and $CaSiO_3$ inclusions in superdeep diamonds. In their model, melting occurs as slabs descend and stagnate in the transition zone, and heat up to the carbonated eclogite solidus where they release a low-degree melt. Such low-degree carbonatitic melts from eclogite are expected to be mobile and rich in alkali, and so may act as effective metasomatizing agents. Our data suggest that because of the relatively high partition coefficient we observe between ringwoodite and sodic carbonate melt, that local sodium enrichment in ringwoodite-bearing mantle may occur in the deep transition zone as a consequence of metasomatic reactions.

Eventual movement of this material through solid-state mantle convection or subduction of metasomatised, ringwoodite-bearing mantle into the lower mantle would lead to Na redistribution among mantle phases. Upward movement in the transition zone may results in further melting of alkali- and carbon-rich material through redox melting (e.g., Rohrbach and Schmidt 2011), leading to further metasomatic reactions. Such metasomatism might be a

mechanism for the growth of distinct mantle chemical and isotopic reservoirs (e.g., Jackson and Dasgupta 2008). In contrast, downward movement of Na-rich ringwoodite bearing material into the lower mantle would result in redistribution of sodium by partitioning between bridgmanite, Ca-perovskite and ferropericlase, all of which can accommodate Na_2O at wt% levels. This process might be a mechanism for alkali enrichment in the upper part of the lower mantle.

ACKNOWLEDGMENTS

The paper benefited by the official reviews made by Anton Shatskiy and one anonymous reviewer. Thanks are also due to the Editor Ian Swainson for his efficient handling of the manuscript. The research was supported by "progetto di Ateneo 2013, University of Firenze" to LB, by C.N.R., Istituto di Geoscienze e Georisorse sezione di Firenze, Italy, the Russian Foundation for Basic Research (project no. 15-55-50033 YaF) to ES and AB. AT thanks Geodynamics Research Center, Ehime University, Matsuyama, Japan, for support of her visit in 2014. OT acknowledges support through the NNSA cooperative agreement #DE-NA0001982 under the Stewardship Science Academic Alliances program.

REFERENCES CITED

Bulanova, G.P., Walter, M.J., Smith, C.B., Kohn, S.C., Armstrong, L.S., Blundy, J., and Gobbo, L. (2010) Mineral inclusions in sublithospheric diamonds from Collier 4 kimberlite pipe, Juina, Brazil: subducted protoliths, carbonated melts and primary kimberlite magmatism. Contributions to Mineralogy and Petrology, 160, 489–510.

Dobson, D.P., and Jacobsen, S.D. (2004) The flux growth of magnesium silicate perovskite single crystals. American Mineralogist, 89, 807–811.

Gregoire, M., Bell, D.R., and Le Roex, A.P. (2002) Trace element geochemistry of phlogopite-rich mafic mantle xenoliths: their classification and their relationship to phlogopite-bearing peridotites and kimberlites revisited. Contributions to Mineralogy and Petrology, 142, 603–625.

Haggerty, S.E. (1983) The mineral chemistry of new titanates from the Jagersfontein kimberlite, South-Africa – Implications for metasomatism in the upper mantle. Geochimica et Cosmochimica Acta, 47, 1833–1854.

Harte, B. (2010) Diamond formation in the deep mantle: the record of mineral inclusions and their distribution in relation to mantle dehydration zones. Mineralogical Magazine, 74, 189–215.

Hazen, R.M., Downs, R.T, and Finger, L.W. (1993) Crystal-chemistry of ferromagnesian silicate spinels – Evidence for Mg-Si disorder. American Mineralogist, 78, 1320–1323.

Hill, R.J., Craig,, J.R., and Gibbs, G.V. (1979) Systematics of the spinel structure type. Physics and Chemistry of Minerals, 4, 317–339.

Ibers, J.A., and Hamilton, W.C., Eds. (1974) *International Tables for X-ray Crystallography*, vol. IV, 366p. Kynock, Dordrecht, The Netherlands.

Ionov, D.A., Griffin, W.L., and O'Reilly, S.Y. (1997) Volatile-bearing minerals and lithophile trace elements in the upper mantle. Chemical Geology, 141, 153–184.

Irifune, T., Kurio, A., Sakamoto, S., Inoue, T., Sumiya. H., and Funakoshi, K. (2004) Formation of pure polycrystalline diamond by direct conversion of graphite at high pressure and high temperature. Physics of the Earth and Planetary Interiors, 143-144, 593–600.

Jackson, M.G., and Dasgupta, R. (2008) Compositions of HIMU, EM1, and EM2 from global trends between radiogenic isotopes and major elements in ocean island basalts. Earth and Planetary Science Letters, 276, 175–186.

Karato, S. (2011) Water distribution across the mantle transition zone and its implications for global material circulation. Earth and Planetary Science Letters, 301, 413–423.

Katsura, T., and Ito, E. (1989) The system Mg_2SiO_4-Fe_2SiO_4 at high pressure and temperatures: precise determination of stabilities of olivine, modified spinel, and spinel. Journal of Geophysical Research, 94, 15663–15670.

Ma, C., Tschauner, O., Beckett, J.R., Liu, Y., Rossman, G.R., Sinogeikin, S.V., Smith, J.S., and Taylor, L.A. (2015) Ahrensite, γ-Fe_2SiO_4, a new shock-metamorphic mineral from the Tissint meteorite: implications for the Tissint shock event on Mars. Geochimica et Cosmochimica Acta, in revision.

Ohtani, E., Litasov, K., Hosoya, T., Kubo, T., and Kondo, T. (2004) Water transport into the deep mantle and formation of a hydrous transition zone. Physics of the Earth and Planetary Interiors, 143-144, 255–269.

O'Neill, H.St.C., and Navrotsky, A. (1983) Simple spinels: crystallographic parameters, cation radii, lattice energies and cation distributions. American Mineralogist, 68, 181–194.

Oxford Diffraction (2006) *CrysAlis* RED (Version 1.171.31.2) and ABSPACK in *CrysAlis* RED. Oxford Diffraction Ltd, Abingdon, Oxfordshire, England.

Pearson, D.G., Brenker, F.E., Nestola, F., McNeill, J., Nasdala, L., Hutchison, M.T., Matveev, S., Mather, K., Silversmit, G., Schmitz, S., Vekemans, B., and Vincze, L. (2014) Hydrous mantle transition zone indicated by ringwoodite included within diamond. Nature, 5047, 221–224.

Robinson, K., Gibbs, G.V., and Ribbe, P.H. (1971) Quadratic elongation: a quantitative measure of distortion in coordination polyhedra. Science, 172, 567–570.

Rohrbach, A., and Schmidt, M.W. (2011) Redox freezing and melting in the Earth's deep mantle resulting from carbon–iron redox coupling. Nature, 472, 209–212.

Sheldrick, G.M. (2008) A short history of SHELX. Acta Crystallographica, A64, 112–122.

Smyth, J.R., Holl, C.M., Frost, D.J., Jacobsen, S.D., Langenhorst, F., and McCammon, C.A. (2003) Structural systematics of hydrous ringwoodite and water in Earth's interior. American Mineralogist, 88, 1402–1407.

Walter, M.J., Bulanova, G.P., Armstrong, L.S., Keshav, S., and Blundy, J.D. (2008) Primary carbonatite melt from deeply subducted oceanic crust. Nature, 454, 622–625

Yaxley, G.M., Crawford, A.J., and Green, D.H. (1991) Evidence for carbonatite metasomatism in spinel peridotite xenoliths from western Victoria, Australia. Earth and Planetary Science Letters, 107, 305–317.

Ye, Y., Brown D.A., Smyth, J.R., Panero, W.R., Jacobsen, S.D., Chang, Y.Y., Townsend, J.P., Thomas, S.M., Hauri, E.H., Dera, P., and Frost, D.J. (2012) Compressibility and thermal expansion of hydrous ringwoodite with 2.5(3) wt% H_2O. American Mineralogist, 97, 573–582.

Yoshino, T., Manthilake, G., Matsuzaki, T., and Katsura, T. (2008) Dry mantle transition zone inferred from the conductivity of wadsleyite and ringwoodite. Nature, 451, 326–329.

FIGURE CAPTIONS

FIGURE 1. SEM-BSE image of idiomorphic crystals of Na-ringwoodite (Na-rgw) associated with Na-bridgmanite (Na-brg), minor periclase and quenched carbonate-silicate melt in the interstitials in the experimental run studied (P = 24 GPa, T = 1700 °C). CamScan electronic microscope MV2300.

FIGURE 2. Na contents (in atoms per formula unit) in ringwoodite and bridgmanite plotted against the Mg contents (in atoms per formula unit).

FIGURE 3. Relation between Δu and u_{obs} for spinel structures [present data, ahr60 (Ma et al. 2015), rgw80 and rgw100 (Hazen et al. 1993 and references therein) given as black stars]. Dashed line: predicted trend according to Hill et al. (1979). Almost all oxide and thiospinels obey this trend. Deviations indicate displacement of the cation from 16*d* or 8*a* sites. In case of Na-rich ringwoodite, the displacement occurs for site 16*d* (Si + Na) and is statistical rather than a static, ordered displacement by structural symmetry reduction.

TABLE 1. Electron microprobe analyses (means and standard deviations in wt% of oxides) and atomic ratios (on the basis of 4 and 3 oxygen atoms for ringwoodite and bridgmanite, respectively) for the phases in the experimental run.

	Na-rgw1	Na-rgw2	Na-rgw3	Na-brg1	Na-brg2
SiO_2	45.68(21)	45.12(26)	44.03(25)	56.84(20)	59.60(23)
Al_2O_3	n.d.	n.d.	n.d.	2.62(9)	1.39(4)
MgO	48.28(22)	51.97(17)	54.78(23)	38.84(15)	38.24(18)
FeO	n.d.	n.d.	n.d.	n.d.	n.d.
Na_2O	4.38(11)	2.63(9)	1.32(10)	1.54(7)	0.52(6)
Tot	99.24	99.72	100.13	99.83	99.75
Si	1.10(2)	1.06(2)	1.03(2)	0.96(3)	0.95(3)
Al	-	-	-	0.05(2)	0.03(2)
Mg	1.70(1)	1.82(2)	1.91(1)	0.98(2)	1.00(2)
Fe	-	-	-	-	-
Na	0.20(2)	0.12(3)	0.06(2)	0.05(2)	0.02(2)

n.d. = not detected

TABLE 2. Data and experimental details for the selected Na-rgw1 crystal

Crystal data	
Formula	$(Mg_{1-3x}Na_{2x}Si_x)_2SiO_4$ (x = 0.050)
Crystal size (mm)	0.021 × 0.034 × 0.038
Form	block
Colour	transparent
Crystal system	cubic
Space group	$Fd\bar{3}m$ (#227 – origin 2)
a (Å)	8.0952(3)
V (Å^3)	530.50(3)
Z	8
Data collection	
Instrument	Oxford Diffraction Xcalibur 3
Radiation type	Mo$K\alpha$ (λ = 0.71073 Å)
Temperature (K)	293(2)
Detector to sample distance (cm)	6
Number of frames	966
Measuring time (s)	150
Maximum covered 2θ (°)	73.78
Absorption correction	multi-scan (ABSPACK; Oxford Diffraction 2006)
Collected reflections	9025
Unique reflections	86
Reflections with $F_o > 4\,\sigma\,(F_o)$	67
R_{int}	0.0265
R_σ	0.0360
Range of h, k, l	$-8 \le h \le 7$, $-10 \le k \le 9$, $-13 \le l \le 13$
Refinement	
Refinement	Full-matrix least squares on F^2
Final R_1 [$F_o > 4\,\sigma\,(F_o)$]	0.0319
Final R_1 (all data)	0.0321
Number of least squares parameters	7
Goodness of Fit	0.98
$\Delta\rho_{max}$ (e Å^{-3})	0.36
$\Delta\rho_{min}$ (e Å^{-3})	-0.81

TABLE 3. Atom coordinates, displacement parameters (Å^2), bond distances (Å) and angles (°) for Na-rgw1.

	x	*y*	*z*	U_{iso}/U_{eq}		
Mg	1/2	1/2	1/2	0.0093(3)		
Si	1/8	1/8	1/8	0.0106(3)		
O	0.24234(17)	0.24234(17)	0.24234(17)	0.0204(6)		
	U^{11}	U^{22}	U^{33}	U^{12}	U^{13}	U^{23}
Mg	0.0093(3)	U^{11}	U^{11}	-0.0009(2)	U^{12}	U^{12}
Si	0.0106(3)	U^{11}	U^{11}	0	U^{12}	U^{12}
O	0.0204(6)	U^{11}	U^{11}	-0.0010(4)	U^{12}	U^{12}

Mg-O	2.088(1)	O-Mg-O	93.35(7)
V (Å^3)	12.07	O-Mg-O	86.65(7)
σ^2	12.26	O-Mg-Mg	46.73(4)
λ	1.0036	O-Mg-Mg	133.27(4)
Si-O	1.645(2)	O-Mg-Mg	92.41(5)
V (Å^3)	2.286	O-Mg-Mg	87.59(5)
Mg-Mg	2.8621(1)	Si-O-Mg	127.67(5)
		Mg-O-Mg	86.54(7)

Quadratic elongation (λ) and angle variance (σ^2) calculated according to Robinson et al. (1971).

Figure 1

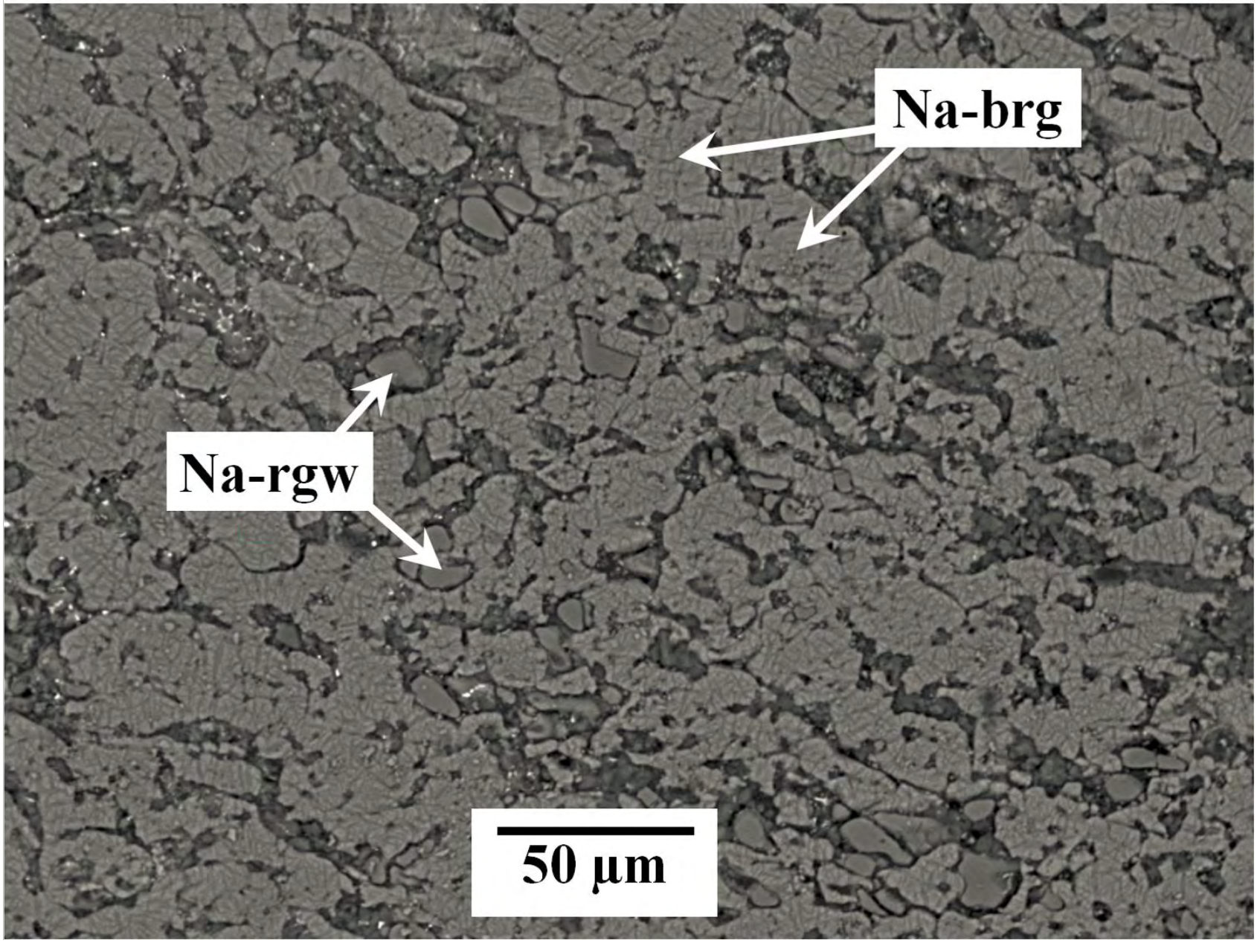

Figure 2

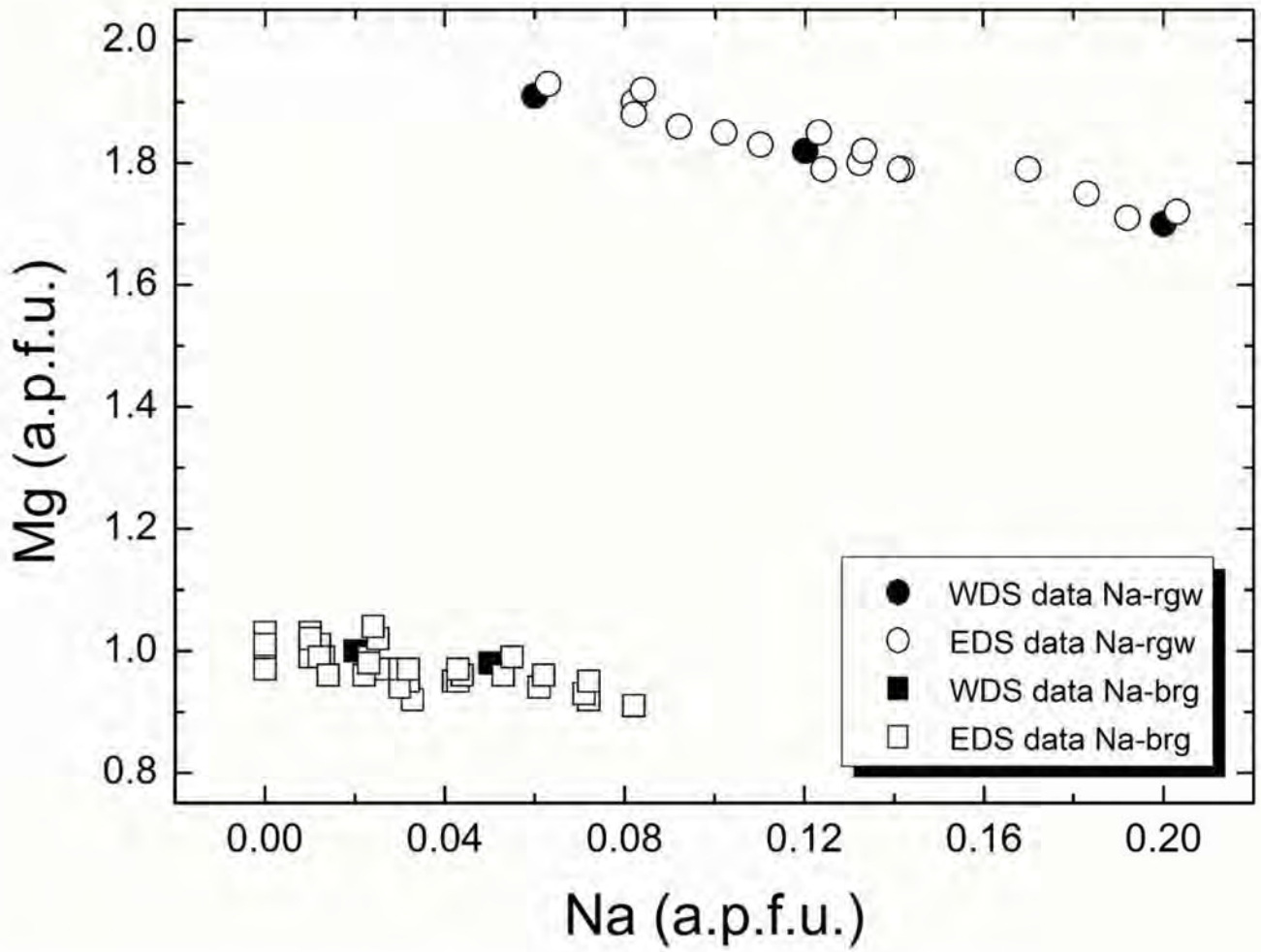
2.0
1.8
1.6
1.4
1.2
1.0
0.8
Mg (a.p.f.u.)
0.00
0.04
0.08
0.12
0.16
0.20
Na (a.p.f.u.)
WDS data Na-rgw
EDS data Na-rgw
WDS data Na-brg
EDS data Na-brg

Figure 3

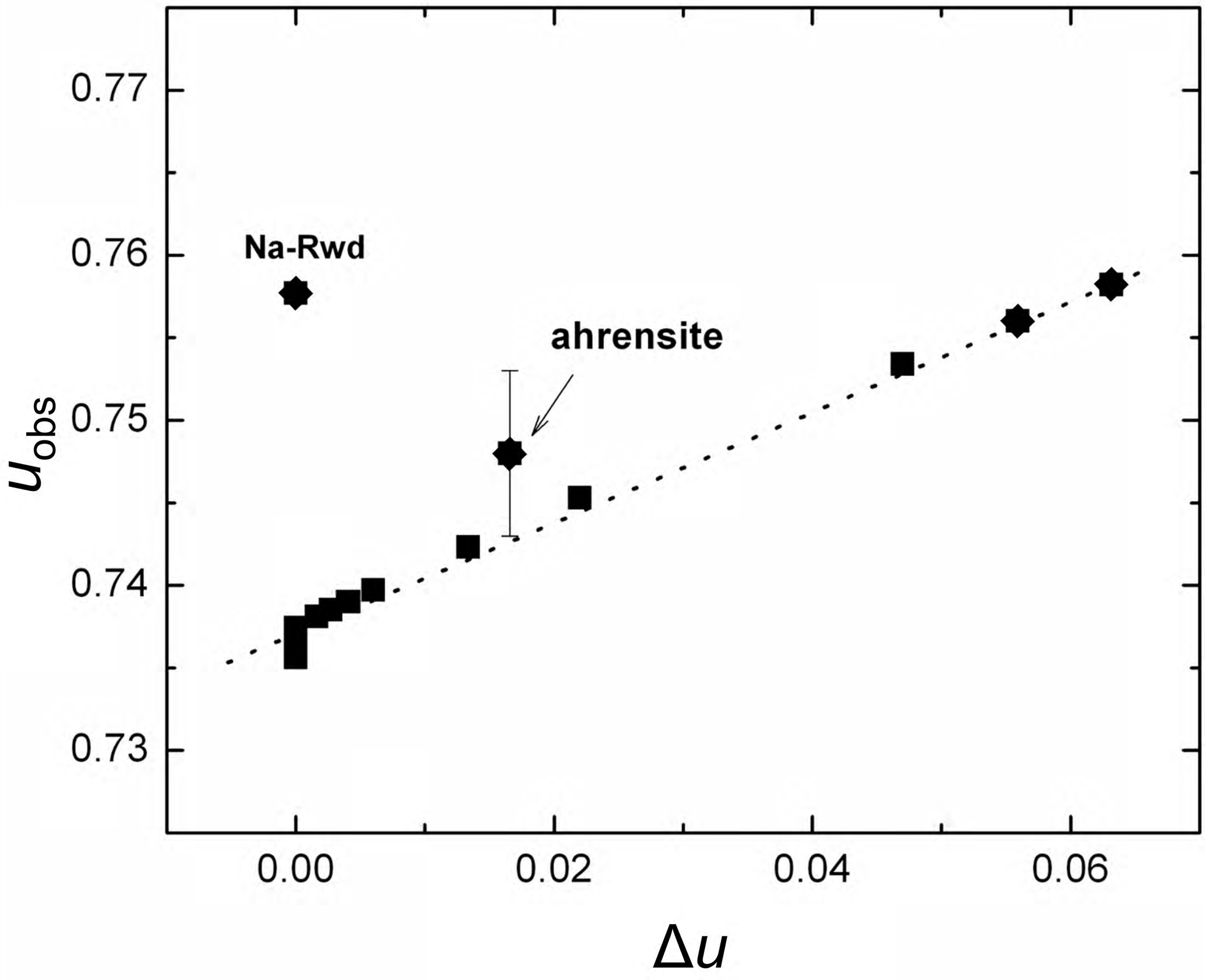
0.77
0.76
0.75
0.74
0.73
u_{obs}
Na-Rwd
ahrensite
0.00
0.02
0.04
0.06
Δu